

# The immersed boundary method: an accelerated SIMPLE approach for moving bodies

Rachel Yovel<sup>a</sup>, Eran Treister<sup>a</sup>, Yuri Feldman<sup>b,\*</sup>

<sup>a</sup>*Department of Computer Sciences, Ben-Gurion University of the Negev, Beer-Sheva, Israel.*

<sup>b</sup>*Department of Mechanical Engineering, Ben-Gurion University of the Negev, Beer-Sheva, Israel.*

---

## Abstract

We present a novel and scalable approach to accelerate a direct-forcing IBM for moving boundary simulations. Building upon the SIMPLE approach, we keep the pressure and forces coupled, formulate the pressure-forces corrections system, solve for pressure-forces corrections, then perform a projection-correction step for velocities followed by a correction step for pressure and forces. To solve the pressure-forces system, we apply a block reduction and suggest an efficient preconditioning approach that is based on using the Laplacian as a preconditioner for the resulting Schur complement. The Laplacian, being independent of the coordinates of the immersed body, is factorized only once (using an efficient direct method) and is then reused throughout the simulation. We present a rigorous proof of the spectral equivalence of the Laplacian and the Schur complement, thereby showing that the preconditioner's efficiency is independent of the grid resolution.

The performance of the method is validated through simulations of the flow around a periodically oscillating sphere in a three-dimensional box. The methodology is then applied to analyze flows generated by arrays of 7 and 14 sub-spheres modeling porous spheres of different porosities. We show good scalability of the algorithm in terms of computational time and memory consumptions. That is, the iteration count for the preconditioned pressure-forces system is nearly constant, regardless of the grid resolution, Reynolds number, and the number of spheres. The developed approach enables accurate moving boundary simulations to be performed on standard workstations, thereby enhancing accessibility of the simulations to the CFD community.

*Keywords:* Moving boundary simulations, Implicit immersed boundary method, Schur complement, Preconditioning

---

## 1. Introduction

The immersed boundary method (IBM), introduced about 50 years ago by Peskin [1], remains a popular approach in investigations of fluid-structure interactions (FSI) for handling boundary conditions at the interfaces of bodies with complex geometries immersed in a fluid. The IBM is applicable to a wide range of physical and biological problems, including flow around solid bodies or inside elastic compartments, and particulate and two-phase immiscible flows, to name but a few. For a comprehensive overview, see the recent review [2] and references therein.

Among all the IBM variants, the direct-forcing approach [3, 4] has gained prominence in recent decades. Its popularity stems from the simplicity of mesh formation and the ability to directly impose no-slip constraints, without the need for assumptions regarding system dynamics. In the direct forcing approach, flow variables are discretized on a regular (Eulerian) grid, while the forces applied by the body on the surrounding flow are discretized on a curved (Lagrangian) grid attached to the body surface. Closure of the overall

---

\*Corresponding author

*Email addresses:* yovelr@bgu.ac.il (Rachel Yovel), erant@cs.bgu.ac.il (Eran Treister), yurifeld@bgu.ac.il (Yuri Feldman)

system is achieved by adding no-slip kinematic constraints. Since the Eulerian and Lagrangian grids do not necessarily coincide, there is a need to define two adjoint operators—interpolation and regularization—to enable information transfer between the two grids. The interpolation operator transfers velocities from the Eulerian to the Lagrangian grid, while the regularization operator smears the Lagrangian body forces over the adjacent Eulerian grid.

Many extensions of the original direct-forcing IBM have been suggested over the years, e.g. for obtaining high-order accuracy in satisfying no-slip constraints [5, 6, 7, 8] for better fulfilling the divergence-free condition [9], for application of the method on unbounded domains [10], and for enforcing the immersed boundary conditions only on one side of the immersed boundary by using Heaviside functions [11]. However, even in the original low-order IBMs, there is a need for a fast method to solve the resulting discrete system, especially for large 3D configurations hosting moving bodies: since the velocities, pressure, and kinematic and dynamic constraints in such a system are coupled at each time step, the system is very large and ill-conditioned, and a monolithic solution is not practical. A variety of approaches have been suggested to address this problem; these include fully explicit [1], fully implicit, and semi-implicit approaches [12, 13, 14, 15, 16], and projection methods [17, 18].

Among these approaches, the immersed boundary projection method [17] keeps the pressure and forces coupled and applies a projection method to the velocity field. An intermediate velocity field is used to construct a modified Poisson equation on the pressure and forces, and a projection step is then applied on the velocity to enforce the divergence-free constraints. To accelerate the solution, the modified Poisson equation is formed by using a Taylor expansion in time rather than a direct inverse of the leading block. However, the modified Poisson equation remains ill-conditioned, becoming particularly restrictive for 3D problems with a high grid resolution. Furthermore, efficient methods available for solving standard Poisson equations on structured grids cannot be fully leveraged for this formulation. In [15], an alternative approach is proposed, employing a Schur complement reduction to implicitly couple the non-solenoidal velocity and Lagrangian force fields, followed by a standard projection-correction procedure to obtain the correct pressure and divergence-free velocity fields. Unfortunately, the method requires a very long pre-computing time (about two weeks) for moving bodies, and extensive storage space for the pre-computed LU factors of the Schur complements that varies for each time step.

Recently, the SIMPLE-based approach for IBM was suggested in [16]. There, an intermediate velocity field is first calculated by solving the momentum equation. Thereafter, a generalized saddle-point system is formulated, consisting of a Poisson equation for the pressure corrections field coupled with an equation on the forces corrections field, that enforces the kinematic no-slip constraints on the surface of the immersed body. This saddle-point matrix is equivalent to the matrix that appears in the modified Poisson equation in [17], for the case of a first-order Taylor approximation. The pressure-forces corrections system is solved in [16] by a block reduction which yields the forces corrections field, from which the pressure corrections field is then obtained. The main drawback of this method is that it is prohibitively expensive when applied to moving-boundary configurations, since the Schur complement which constitutes the force corrections equation changes at each time step.

In this work, we adapt the SIMPLE approach [16] to accommodate moving boundary configurations. We achieve a significant reduction in computational time and a notably low memory usage. The pressure-forces corrections system—whose solution constitutes the computational bottleneck—is solved by taking the primal Schur complement, rather than the dual Schur complement used in [16], i.e., obtaining the pressure corrections field first, from which the force-corrections field is then computed. In this way, the overall complexity of the solution is significantly reduced by virtue of the approximation of the regularization block by a scalar matrix, as suggested in [16]. To further improve the conditioning and to enhance the scalability of the overall method through the solution of the pressure-corrections equation, we have developed a novel preconditioning approach, in which the Laplacian is taken as a preconditioner for the primal Schur complement of the pressure-forces corrections system. In other words, we solve the pressure corrections equation by using a preconditioned Krylov method, in which each iteration requires the solution of a single Poisson equation. Thanks to the special structure of the Laplacian on a regular grid, the Poisson equation is solved by a fast direct method [19, 20]. Moreover, since the Laplacian matrix is constant throughout the

time steps, it needs to be factorized only once at the beginning of the computation.

Overall, our accelerated SIMPLE-based IBM shows promising scaling properties in terms of memory consumption and computational time. We prove rigorously and demonstrate numerically that the conditioning properties of the suggested preconditioning approach does not depend on the grid size or other system parameters. We demonstrate the potential advantages of our approach by applying it to the numerical simulation of the flow developing around a periodically oscillating sphere immersed within a 3D box. The methodology is further utilized to investigate more complex flows generated by arrays of 7 and 14 sub-spheres modeling porous spheres with different porosities. We thereby show that our method is suitable for performing realistic moving boundary simulations on standard workstations.

## 2. Background

### 2.1. Governing equations and discretization

The incompressible flow around an immersed body is governed by the non-dimensional Navier-Stokes equations, complemented by no-slip constraints on the body's surface:

$$\frac{\partial \mathbf{u}}{\partial t} + (\mathbf{u} \cdot \nabla) \mathbf{u} = -\nabla p + \frac{1}{Re} \nabla^2 \mathbf{u} + \mathbf{f} \quad \forall \vec{x} \in \Omega, \quad (1)$$

$$\nabla \cdot \mathbf{u} = 0 \quad \forall \vec{x} \in \Omega, \quad (2)$$

$$\mathbf{u} = \mathbf{U}^\Gamma \quad \forall \vec{x} \in \Gamma, \quad (3)$$

$$\text{BC} \quad \forall \vec{x} \in \partial\Omega, \quad (4)$$

where  $\Omega$  is a domain,  $\Gamma \subset \Omega$  is the boundary of the immersed body (or bodies),  $p = p(\vec{x}, t)$  is the pressure,  $\mathbf{f} = \mathbf{f}(\vec{x}, t)$  reflects the impact of immersed body on surrounding flow,  $\mathbf{u}$  is the flow velocity, and  $\mathbf{U}^\Gamma$  is the velocity of the surface of the immersed body. The normalized equations (1), (2) and (3) are governed by a single non-dimensional parameter: the Reynolds number,  $Re = U_0 L / \nu$  where  $\nu$  is the kinematic viscosity and  $L$  and  $U_0$  are the characteristic length and velocity, respectively. The time, pressure and force density are normalized by utilizing the scales  $L/U_0$ ,  $\rho U_0^2$  and  $\rho U_0^2 / L$ , respectively, where  $\rho$  is the fluid density.

The flow velocity and pressure, constituting the Eulerian variables, are discretized on a staggered grid: pressure is stored at cell centers, while velocity components are located at the corresponding face centers. The spatial derivatives are discretized using a standard central second-order finite volumes scheme. The time derivative is discretized by a backward second order finite differences scheme.

Following the IBM formalism, the surface of immersed body is determined by a series of discrete points, constituting the Lagrangian grid, see Fig. 1. For numerical stability, the distance between adjacent Lagrangian points should be approximately equal to the Eulerian cell size. Variables on the Lagrangian grid are denoted by capital letters, e.g.,  $\mathbf{F}$  corresponds to the Lagrangian forces discretized at the Lagrangian points.

Since the Eulerian and Lagrangian grids do not necessarily coincide, two adjoint operators are next introduced to facilitate the data transfer between them: the regularization operator  $R$ , which smears the Lagrangian forces onto the underlying Eulerian grid, and the interpolation operator  $R^T$ , which interpolates the Eulerian velocities to Lagrangian points. These operators are defined by utilizing the following discrete Dirac delta function, proposed in [21]:

$$\delta(r) = \begin{cases} \frac{1}{6\Delta r} \left( 5 - 3\frac{|r|}{\Delta r} - \sqrt{-3\left(1 - \frac{|r|}{\Delta r}\right)^2 + 1} \right) & \text{for } 0.5\Delta r < |r| \leq 1.5\Delta r, \\ \frac{1}{3\Delta r} \left( 1 + \sqrt{-3\left(\frac{|r|}{\Delta r}\right)^2 + 1} \right) & \text{for } |r| \leq 0.5\Delta r, \\ 0 & \text{otherwise,} \end{cases} \quad (5)$$

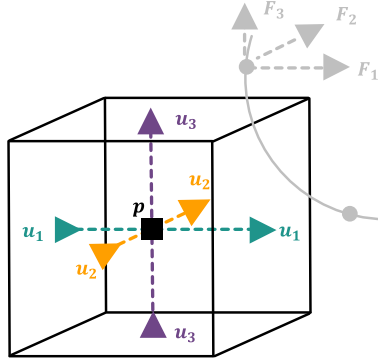


Figure 1: An Eulerian discretization cell in 3D and two adjacent Lagrangian points on the surface of the immersed body.

where  $r$  represents the distance from the smeared point and  $\Delta r$  represents the cell width in the  $r$  direction. This delta function gained popularity over the years [22, 23, 17, 16], due to its compact support of at most three discretization cells in each direction.<sup>1</sup>

The regularization and interpolation operators are then defined, using the discrete Dirac delta function from Eq. (5), by

$$\mathbf{U}_k^\Gamma = (R^T \mathbf{u})_k = \Delta x^3 \sum_i \mathbf{u}_i \delta^3(\mathbf{X}_k - \mathbf{x}_i), \quad (6)$$

$$\mathbf{f}_i = (R\mathbf{F})_i = \Delta x^3 \sum_k \mathbf{F}_k \delta^3(\mathbf{x}_i - \mathbf{X}_k), \quad (7)$$

where  $\mathbf{x}_i$  are the coordinates of the  $i$ -th velocity location, and  $\mathbf{X}_k$  is the  $k$ -th Lagrangian point. The notation  $\delta^3$  corresponds to the discrete Dirac delta function applied in 3D. As long as we use the same delta function for the interpolation and the regularization, the two operators are transpose of each other in matrix representation. To facilitate the notation, we denote by  $R$  the regularization and by  $R^T$  the interpolation operator.

## 2.2. The SIMPLE approach for IBM

We recall that the SIMPLE algorithm [24] for solution of the Navier-Stokes equations starts with a prediction step for the calculation of an intermediate velocity field  $\mathbf{u}^*$ , which is subsequently used in the calculation of the corrections for the pressure  $p'$  and velocity  $\mathbf{u}'$  fields. The final stage of the algorithm comprises the correction step  $p^{(n+1)} = p^{(n)} + p'$  for calculating the pressure field, and the projection step  $\mathbf{u}^{(n+1)} = \mathbf{u}^* + \mathbf{u}'$  for calculating the divergence-free velocity field.

In [16], the SIMPLE approach is extended to the immersed boundary framework by introducing a La-

<sup>1</sup>Since the discrete Dirac delta function in Eq. (5) provides only a first order of spatial accuracy, other delta functions can be also considered to improve the accuracy (with the price of less favorable sparsity), see [6].

garngian forces field  $\mathbf{F}^{(n+1)} = \mathbf{F}^{(n)} + \mathbf{F}'$  and solving the following (semi-discretized) system of equations:

$$\frac{3\mathbf{u}^* - 4\mathbf{u}^{(n)} + \mathbf{u}^{(n-1)}}{2\Delta t} = -\nabla p^{(n)} + \frac{1}{Re}\nabla^2\mathbf{u}^* + R\mathbf{F}^{(n)} - (\mathbf{u} \cdot \nabla\mathbf{u})^{(n)} \quad (8)$$

$$\frac{3\mathbf{u}'}{2\Delta t} = -\nabla p' + R\mathbf{F}' \quad (9)$$

$$R^T\mathbf{u}^{(n+1)} = \mathbf{U}^\Gamma \quad (10)$$

$$\nabla \cdot \mathbf{u}^{(n+1)} = 0 \quad (11)$$

where  $R$  is the regularizaton operator defined in Eq. (7), that smears the forces from the Lagrangian points to the adjacent Eulerian velocity locations by utilizing the discrete Dirac delta function proposed in [21],  $R^T$  is the adjoint interpolation operator, defined in Eq. (6), that interpolates the intermediate velocity field onto the corresponding Lagrangian points, and  $\mathbf{U}^\Gamma$  is the velocity value on the surface of the immersed body.

First, the intermediate velocity field  $\mathbf{u}^*$  is obtained from the solution of Eq. (8). We note that this velocity field does not necessarily satisfy the no-slip and divergence-free constraints. Second, a divergence is applied on both sides of Eq. (9), similarly to the original SIMPLE method, yielding the modified pressure Poisson equation

$$-\nabla^2 p + \nabla \cdot (R\mathbf{F}') = -\frac{3}{2\Delta t}\nabla \cdot \mathbf{u}^*, \quad (12)$$

where the right hand side in this equation is achieved by utilizing the divergence free constraint in Eq. (11), that implies  $\nabla \cdot \mathbf{u}^* = -\nabla \cdot \mathbf{u}'$ . However, Eq. (12) for the pressure corrections is not closed, as it also includes the forces corrections field. Thus, utilizing again Eq. (9) we obtain

$$\mathbf{u}^{(n+1)} = \mathbf{u}^* + \frac{2}{3}\Delta t(-\nabla p' + R\mathbf{F}'). \quad (13)$$

By applying the interpolation  $R^T$  on both sides of Eq. (13) and substituting it back into Eq. (10), we attain the following system of equations governing the corrections for the pressure and forces fields:

$$\begin{bmatrix} L & B^T \\ B & -C \end{bmatrix} \begin{bmatrix} p' \\ \mathbf{F}' \end{bmatrix} = \begin{bmatrix} G^T G & G^T R \\ R^T G & -R^T R \end{bmatrix} \begin{bmatrix} p' \\ \mathbf{F}' \end{bmatrix} = \begin{bmatrix} RHS_{p'} \\ RHS_{\mathbf{F}'} \end{bmatrix} \quad (14)$$

where  $G$  is the discretized gradient,  $RHS_{p'} = -\frac{3}{2\Delta t}\nabla \cdot \mathbf{u}^*$  and  $RHS_{\mathbf{F}'} = \frac{3}{2}\frac{R^T\mathbf{u}^* - \mathbf{U}^\Gamma}{\Delta t}$ . This system was solved in [16] by the block reduction

$$S_d\mathbf{F}' = BL^{-1}RHS_{p'} - RHS_{\mathbf{F}'} \quad (15)$$

$$p' = L^{-1}(RHS_{p'} - B^T\mathbf{F}'), \quad (16)$$

where  $S_d$  is the dual Schur-complement:

$$S_d := C + BL^{-1}B^T. \quad (17)$$

Their approach yielded the  $\mathbf{F}'$  field by solving Eq. (15) via either direct [25] or Krylov iteration [26] solvers, followed by calculation of the  $p'$  field by Eq. (16). While  $S_d$  is relatively small, constructing it for realistic 3D configurations requires applying the Laplacian solver hundreds of thousands of times (for each column of  $B^T$ , corresponding to a Lagrangian point). Although this task is feasible as a precomputing step for stationary immersed bodies, it becomes impractical for moving boundary simulations where  $B^T$  changes at each time step.

### 3. Method

#### 3.1. The Laplacian as a preconditioner

To accelerate the suggested method and adjust it for moving boundary simulations, we propose the following remedy: instead of forming the *dual* Schur complement, we form the *primal* Schur complement

$$S_p := L + B^T C^{-1} B, \quad (18)$$

and solve the resulting decoupled system of equations, first for the pressure  $p'$  and then for the force  $\mathbf{F}'$  corrections fields:

$$S_p p' = R H S_{p'} + B^T C^{-1} R H S_{\mathbf{F}'} \quad (19)$$

$$\mathbf{F}' = C^{-1} (B p' - R H S_{\mathbf{F}'}). \quad (20)$$

Forming the primal Schur complement  $S_p$  and calculating the right hand side in Eq. (19) and (20) is significantly cheaper than forming the dual Schur complement  $S_d$  and calculating the right hand side in Eq. (15) and (16): in the virtue of the scalar approximation  $C \approx \frac{1}{2}I$ , that was suggested in [16], we avoid calculating  $C^{-1}$  and use the approximation  $C^{-1} \approx 2I$  and

$$S_p \approx \tilde{S}_p := L + 2B^T B. \quad (21)$$

This approximation is valid for immersed bodies with sufficiently smooth surfaces and improves with increasing grid resolution. After applying this scalar approximation on both Eq. (19) and (20), we obtain

$$\tilde{S}_p p' = R H S_{p'} + 2B^T R H S_{\mathbf{F}'} \quad (22)$$

$$\mathbf{F}' = 2(B p' - R H S_{\mathbf{F}'}). \quad (23)$$

However, both  $S_p$  and  $\tilde{S}_p$  are ill-conditioned and large, and hence neither a direct nor an iterative solution of Eq. (19) (or the approximated version, Eq. (22)) is practical, and a good preconditioner is required. To this end, we use the Laplacian  $L$  as a preconditioner. We show in the following sections that Eq. (19) can be solved in just a few iterations of a preconditioned Krylov method, because  $L$  and  $S_p$  are spectrally equivalent. That is, we prove in Section 4 that the eigenvalues of the preconditioned operator  $L^{-1}S_p$  lie in a narrow constant interval, that does not depend neither on the physical variables nor on the grid size. As long as  $\tilde{S}_p$  well approximates  $S_p$ , this result nearly holds for the preconditioned operator  $L^{-1}\tilde{S}_p$ , and as we show numerically in Section 5, Eq. (22) can be solved in just a few iterations. Since the solution of the pressure-forces corrections system comprises the computational bottleneck, our preconditioning approach enables a fast solution of the problem as a whole, and favorable scalability properties.

The resulting method is summarized in Alg. 1.

---

**Algorithm 1:** accelerated SIMPLE for IBM.

---

1. Solve Eq. (8) for  $\mathbf{u}^*$ .
  2. Solve Eq. (22) iteratively, using a Krylov iteration based method preconditioned by  $L$ , for  $p'$ .
  3. Substitute the obtained  $p'$  in Eq. (23), and calculate  $\mathbf{F}'$ .
  4. Complete the pressure correction  $p^{(n+1)} = p^{(n)} + p'$ .
  5. Compute  $\mathbf{u}'$  by substituting the obtained  $p'$  and  $F'$  into Eq. (9).
  6. Complete the velocity projection step  $\mathbf{u}^{(n+1)} = \mathbf{u}^* + \mathbf{u}'$ .
- 

**Remark 3.1.** *There is abundance of literature on block-preconditioning for saddle point matrices as appears in Eq. (14), mainly by Schur complement preconditioning. Since forming and inverting the exact Schur-complement is computationally expensive, broad research is dedicated to the search of cheap approximations*

for the inverse of the Schur-complement, see [27]. Our method offers an efficient approximation for the primal Schur complement for a certain class of saddle point matrices, and can be implemented either by Alg. 1 or by a corresponding block lower triangular Schur complement preconditioner.

### 3.2. Implementation details

In this subsection we describe our efficient matrix-free implementation. First, the operator  $B^T$  consists of the (minus) divergence applied to the discrete Dirac delta function's weight terms obtained by Eq. (5). A matrix free implementation allows efficient shared-memory parallelization (we used OpenMP) and enables rapid re-computation of these operators at each time step. Second, for each step of the preconditioned Krylov iteration, only a matrix-vector product against the preconditioned operator is needed. We use left preconditioning, which is mathematically equivalent to solving Eq. (22) with both sides multiplied by  $L^{-1}$  from the left. However, we don't need to form  $L^{-1}$ , nor to apply a Laplacian solver at multiple columns, in order to perform a preconditioning step. Since the matrix of the preconditioned system is

$$L^{-1}\tilde{S}_p = I_m + 2L^{-1}B^TB,$$

where  $I_m$  is an identity matrix of the appropriate size, the product of  $L^{-1}\tilde{S}_p$  with a vector  $\mathbf{v}$  can be conveniently obtained with the direct solver suggested in [19] applied, only once, on the vector  $B^T(B\mathbf{v})$ . Employing Intel MKL routines<sup>2</sup> enables efficient calculation of the sparse matrix-vector products. Note that since the scalar approximation for  $C^{-1}$  is used, the calculation of the second term in Eq. (22) and of the entire Eq. (23) are trivial, as they both require a single matrix-vector product.

Finally, we discuss the factorization of the preconditioner  $L$ . It was suggested in [19] that any matrix that can be written as a sum of Kroncker products of smaller matrices with identity matrices can be factorized by utilizing an eigen-decomposition of each of the small matrices. As shown there, the system can be solved with a complexity of  $O(n^{4/3})$  for a regular 3D grid. The computational cost can be further reduced by utilizing the Thomas TDMA algorithm in one of the three directions. For transient problems this method is highly efficient, as shown in [20], because the corresponding operators can be factorized in advance and used in each time step.

## 4. Theory: a spectral bound on the preconditioned system

In this section, we justify taking the Laplacian as a preconditioner for the primal Schur complement (18) of the coupled pressure-forces system (14). A good preconditioner should resemble the original matrix, in the sense of spectral equivalence, i.e., the spectrum of the preconditioned system should be bounded. Theorem 4.1 shows this property.

**Theorem 4.1.** *For every generalized saddle-point matrix of the form*

$$\begin{bmatrix} L & B^T \\ B & -C \end{bmatrix} = \begin{bmatrix} G^T G & G^T R \\ R^T G & -R^T R \end{bmatrix}, \quad (24)$$

where  $G$  is an  $n \times m$  matrix and  $R$  an  $n \times k$  matrix<sup>3</sup>, the leading block  $L$  is spectrally equivalent to the primal Schur complement  $S_p$  from Eq. (18), in the sense

$$\text{spec}(L^{-1}S_p) \subseteq [1, 2]. \quad (25)$$

*Proof.* It is readily seen that

$$L^{-1}S_p = I_m + L^{-1}B^TC^{-1}B$$

<sup>2</sup>We convert  $B$  and  $B^T$  to the CSR format at each time step for further utilization of Intel MKL routines.

<sup>3</sup>Typically,  $n > m > k$ , but this assumption is not necessary for the Theorem's statement.

where  $I_m$  stands for the identity matrix of size  $m \times m$ . Hence, it is sufficient to show that

$$\text{spec}(L^{-1}B^TC^{-1}B) \subseteq [0, 1],$$

or equivalently, that the generalized eigenvalue problem

$$B^TC^{-1}B\mathbf{v} = \lambda L\mathbf{v} \tag{26}$$

has only solutions that satisfy  $\lambda \in [0, 1]$ . To bound  $\lambda$ , we bound the generalized Rayleigh quotient

$$\frac{\langle B^TC^{-1}B\mathbf{v}, \mathbf{v} \rangle}{\langle L\mathbf{v}, \mathbf{v} \rangle} = \frac{\langle G^TPG\mathbf{v}, \mathbf{v} \rangle}{\langle G^TG\mathbf{v}, \mathbf{v} \rangle} = \frac{\langle PG\mathbf{v}, G\mathbf{v} \rangle}{\langle G\mathbf{v}, G\mathbf{v} \rangle}, \quad \mathbf{v} \in \mathbb{R}^m \tag{27}$$

where  $P := R(R^TR)^{-1}R^T$  is an orthogonal projector (namely,  $P^2 = P$  and  $P^T = P$ ). Hence, the only eigenvalues of  $P$  are 0 and 1, and  $\text{Null}(P) = \text{Range}(P)^\perp$ , see, e.g., [28]. Particularly, every vector can be uniquely decomposed into a sum of orthogonal vectors in the nullspace and in the range of  $P$ , e.g., we can write  $G\mathbf{v} = \mathbf{v}_1 + \mathbf{v}_2$ , where  $\mathbf{v}_1 \in \text{Null}(P)$ ,  $\mathbf{v}_2 \in \text{Range}(P)$  and  $\langle \mathbf{v}_1, \mathbf{v}_2 \rangle = 0$ . Consequently,

$$\langle PG\mathbf{v}, G\mathbf{v} \rangle = \langle P(\mathbf{v}_1 + \mathbf{v}_2), \mathbf{v}_1 + \mathbf{v}_2 \rangle = \langle P\mathbf{v}_1, \mathbf{v}_1 \rangle + 2\langle P\mathbf{v}_1, \mathbf{v}_2 \rangle + \langle P\mathbf{v}_2, \mathbf{v}_2 \rangle = \langle \mathbf{v}_2, \mathbf{v}_2 \rangle = \|\mathbf{v}_2\|^2, \tag{28}$$

where the third equality holds because  $P\mathbf{v}_1 = 0$  and  $P\mathbf{v}_2 = \mathbf{v}_2$ . Finally, we substitute (28) into (27), which yields

$$0 \leq \frac{\langle PG\mathbf{v}, G\mathbf{v} \rangle}{\langle G\mathbf{v}, G\mathbf{v} \rangle} = \frac{\|\mathbf{v}_2\|^2}{\|\mathbf{v}_1 + \mathbf{v}_2\|^2} = \left( \frac{\|P(\mathbf{v}_1 + \mathbf{v}_2)\|}{\|\mathbf{v}_1 + \mathbf{v}_2\|} \right)^2 \leq \|P\|_2^2 = (\rho(P))^2 = 1 \tag{29}$$

where  $\rho(P)$  is the spectral radius of  $P$ , and since  $P$  is symmetric, it is equal to  $\|P\|_2$ .  $\square$

The importance of Theorem 4.1 stems from its generality, i.e., for the spectral equivalence to hold, any discretisation of the gradient and any regularization operator can be considered. The expected scalability and robustness of the method is therefore proved for a large variety of cases, with symmetry being the only limitation, i.e., the divergence must be the transpose of the gradient, and the interpolation must be the transpose of the regularization.

The assumption of symmetry is not particularly restrictive, as it is natural to take the same delta functions for the regularization and interpolation, and the same discretization for the gradient and divergence. In practice, some implementation of the possible BC might lead to a non-symmetric Laplacian. Nevertheless, even when the Laplacian slightly differs from  $G^TG$ , the spectral result of Theorem 4.1 seems to hold in practice, as demonstrated in the next section.

**Remark 4.1.** *As an immediate corollary of Theorem 4.1, the error iteration matrix  $T = I_m - L^{-1}S_p$  of the preconditioned system satisfies  $\rho(T) \leq 1$ . When this inequality is strong, convergence is guaranteed. A Krylov iterative method typically further accelerates the convergence and might converge in just a few iterations even when the spectral radius of the error iteration matrix is even greater than 1. However, the convergence rate of a Krylov iterative method is determined by the scattering of the eigenvalues, which can depend on the specific configuration. In typical cases,  $B$  is extremely rank deficient, because the number of Lagrangian points is very small compared to the number of Eulerian cells. In such a case,*

$$\tilde{S}_p = L + 2B^TB \approx L \tag{30}$$

*and the error iteration matrix has a large null-space, which implies that the eigenvalues are clustered and the Krylov iteration count is low. In the next section, we demonstrate that even when the number of Lagrangian points grows—by taking multiple bodies—the observed iteration count remains low.*

Spectrum's support for the preconditioned system				
Grid size (cells)	24 × 24	48 × 48	96 × 96	192 × 192
$\text{spec}(L^{-1}S_p) \subseteq$	[1,1.9997]	[1,1.9997]	[1,1.9996]	[1,1.9996]
$\text{spec}(L^{-1}\tilde{S}_p) \subseteq$	[1,1.9944]	[1,1.9986]	[1,2.0099]	[1,2.0067]

Table 1: The spectrum's support of the preconditioned system  $L^{-1}S_p$  and the corresponding system with an approximate Schur complement  $L^{-1}\tilde{S}_p$ , obtained for a stationary circular cylinder placed at the center of a 2D lid-driven cavity.

**Remark 4.2.** *A similar result can be proved for a weighted version of the saddle-point matrix, such as*

$$\begin{bmatrix} G^T W G & G^T W R \\ R^T W G & -R^T W R \end{bmatrix}, \quad (31)$$

where  $W$  is SPD, by taking  $\tilde{G} = W^{\frac{1}{2}}G$  and  $\tilde{R} = W^{\frac{1}{2}}R$ . Since such a weighted system appears in [17], it gives rise to a utilization of a similar preconditioning approach in the context of projection methods.

## 5. Results

### 5.1. Verifying the preconditioning method by two-dimensional experiments

The aim of this subsection is to validate the theoretical result of Theorem 4.1 numerically, and to demonstrate certain condition number properties. For convenience in demonstrating these properties, we chose relatively small 2D cases. The numerical experiments were conducted using a model problem consisting of a stationary cylinder placed at the center of a lid-driven cavity. Conditioning analysis was performed on the matrices  $L$ ,  $S_p$  and  $\tilde{S}_p$  obtained from the numerical simulations.

In the first experiment we demonstrate the spectral result of Theorem 4.1, reading  $L^{-1}S_p \subseteq [1, 2]$ . Table 1, which presents the spectrum's support  $[\lambda_{min}, \lambda_{max}]$ , shows that  $\text{spec}(L^{-1}S_p) \subseteq [1, 2]$ , as predicted theoretically. Since the scalar approximation of  $C$  is crucial for the efficiency of our method, we also measure the spectrum's support for  $L^{-1}\tilde{S}_p$ , with  $\tilde{S}_p$  from Eq. (21). In this case, most of the eigenvalues satisfy  $\lambda \in [1, 2]$ , and although some eigenvalues slightly exceed 2, the maximal eigenvalue tends to 2 as the grid resolution increases. It can be explained by that fact that the quality of the scalar approximation  $C \approx \frac{1}{2}I$  improves with the grid resolution, as shown in [16].

In the second experiment, we compare the preconditioned matrix  $L^{-1}\tilde{S}_p$  to the non-preconditioned primal Schur complement  $\tilde{S}_p$ , in terms of the estimated 1-norm condition number. The results in Fig. 2(a) show that the condition number is significantly improved by the preconditioning. We note that the 1-norm condition number is significantly higher than the standard 2-norm condition number, yet easier to estimate numerically. We use the Matlab function `condst` for this estimation.

In the third experiment we compare the GMRES iteration count required for the solution of the original system  $\tilde{S}_p p' = \mathbf{b}$  and the preconditioned system  $L^{-1}\tilde{S}_p p' = L^{-1}\mathbf{b}$ . Note that during a full solution of the problem, the right hand side  $\mathbf{b}$  changes at any time step. Here, we solved the systems for a random right hand side to demonstrate the improvement of the conditioning in terms of iteration count. The results shown in Fig. 2(b) demonstrate that the preconditioned system can be solved in just a few iterations regardless of the grid size, while the original system requires hundreds of iterations for very small grids and thousands for larger grids. This scalability property enables performing the simulations on dense grids, as shown in the next subsection.

### 5.2. Three-dimensional experiments: an oscillating solid sphere

An oscillating solid sphere of diameter  $D$  placed within a  $4D \times 4D \times 6D$  box filled with a quiescent fluid (see Fig. 3(a)) is considered. The sphere oscillates vertically with velocity and position given by:

$$U_z = U_{max} \sin(\omega T), \quad Z = -\frac{U_{max}}{\omega} \cos(\omega T) \quad (32)$$

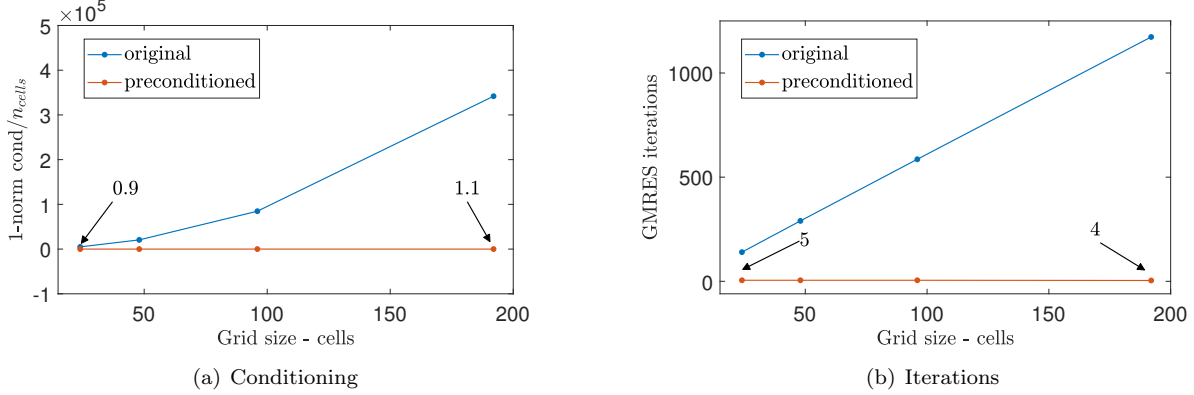


Figure 2: The 1-norm condition number per number of cells of the original and preconditioned matrices for the pressure corrections, and GMRES iteration count required for the solution of a system with a random right-hand-side for the corresponding matrices.

where  $\omega$  is the angular frequency and  $T$  is the time. No-slip boundary conditions are imposed on all solid boundaries, including the surface of the sphere and the walls of the box. To non-dimensionalize the system,  $D$ ,  $U_{max}$ ,  $U_{max}/D$ , and  $\rho U_{max}^2$  are utilized as characteristic scales of length, velocity, time, and pressure, respectively, yielding the following relationships governing the sphere's kinematics:

$$u_z = \sin\left(\frac{D}{A}t\right), \quad z = -\frac{A}{D} \cos\left(\frac{D}{A}t\right) \quad (33)$$

where  $A = U_{max}/\omega$  represents the amplitude of the oscillations. The system's behavior is governed by two non-dimensional parameters: the Reynolds number,  $Re = U_{max}D/\nu$ , and the amplitude ratio,  $A/D$  (where  $D/A$  is also known as the reduced frequency). A snapshot of representative flow including pathlines and contours of the vertical velocity component  $u_z$  around the sphere, typical of the given set-up, is presented in Fig. 3(b).

For completeness, we recall the force balance equation of an accelerating sphere in an otherwise quiescent fluid, as described in [15]. In accordance with the IBM formalism where the sphere is filled with the same fluid as that outside, this equation can be expressed as [29]:

$$\frac{d}{dt} \int_{V_{sph}} \mathbf{u} dV = \mathbf{f}_D + \int_{V_{sph}} \mathbf{f} dV \quad (34)$$

where  $\mathbf{f}_D$  is the instantaneous drag force exerted by the fluid on the sphere and the integral of  $\mathbf{f}$  is the instantaneous external force required to maintain the prescribed kinematics of the body. This external force can be directly computed by summing all the IBM forces:

$$\int_{V_{sph}} \mathbf{f} dV = \sum_{i,j,k} \mathbf{f}_{ijk} \Delta x \Delta y \Delta z. \quad (35)$$

The drag force,  $\mathbf{f}_D$ , can be determined by using Eqs.(34) and (35). Following [30], we assume rigid-body motion of the fluid within the sphere, allowing us to approximate the left-hand side term of Eq. (34) as

$$\frac{d}{dt} \int_{V_{sph}} \mathbf{u} dV = \frac{d\mathbf{u}_c}{dt} V_{sph} \quad (36)$$

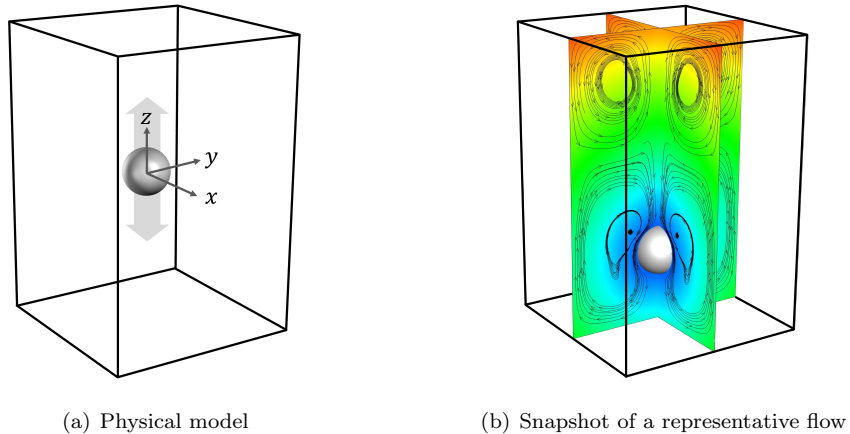


Figure 3: An oscillating sphere of diameter  $D$  and a box of dimensions  $4D \times 4D \times 6D$

where  $d\mathbf{u}_c/dt$  is the acceleration of the sphere's center of mass. For comparison purposes, we express the drag force  $\mathbf{f}_D$  in terms of the drag coefficient for a spherical geometry:

$$\mathbf{C}_D = \frac{8\mathbf{f}_D}{\rho U_{max}^2 \pi D^2}. \quad (37)$$

After scaling the drag force by  $\rho U_{max}^2 D^2$  the  $z$  component of the drag coefficient  $C_D \equiv (C_D)_z$  becomes  $C_D = 8f_{D_z}/\pi$ .

To verify our method, we compare the time evolution and maximum values of the drag coefficient  $C_D$  obtained on a  $400 \times 400 \times 600$  grid for four Reynolds numbers in the range  $50 \leq Re \leq 200$  at  $A/D = 1$  with the corresponding data reported in [15] and [31]. Following the principles outlined in Section 2.1, the immersed boundary is represented by Lagrangian points uniformly distributed with spacing approximately equal to the Eulerian grid size. This uniform distribution was achieved using Leopardi's noniterative method [32], which ensures each Lagrangian point is associated with a virtual surface region of equal area. The comparison of the drag coefficient time evolution is presented in Fig. 4(a), where the results of our current simulations are shown by solid lines, while the reference data reported in [15] are denoted by filled circles. The sphere's position is indicated by a dotted line. Excellent agreement is obtained for the entire range of governing parameters, with the maximum relative deviation not exceeding 2.1%, thus successfully verifying our results. In Fig. 4(b), the maximum drag coefficient values obtained in the present study are compared with the results for the entire range of  $Re$  and  $A/D$  values reported in [31], under the assumption of axisymmetric non-confined flow. The maximum drag coefficients for  $A/D = 0.5, 1$  and  $1.5$  are shown by filled circles, while the results from [31] are denoted by a solid line. The results demonstrate good agreement, with deviations not exceeding 6.7%. The slightly higher values obtained in the present study can be attributed to the presence of walls with no-slip conditions in our setup.

To demonstrate the efficiency of the preconditioner, we measure the average number of BiCGStab iterations required for convergence of the preconditioned system to a  $10^{-12}$  tolerance, for different Reynolds numbers and grid sizes, as shown in Table 2. The average is taken over three different  $A/D$  ratios: 0.5, 1.0, and 1.5, and over four distinct locations of the sphere during its periodic oscillation, i.e., at the lowest point of the stroke (bottom dead center), at the highest point of the stroke (top dead center), and at the two midpoints of the stroke as the sphere moves upwards and downwards. We observe that the iteration count remains nearly constant and remarkably low, regardless of the Reynolds number, grid size,  $A/D$  ratio, and location of the sphere during its oscillatory motion.

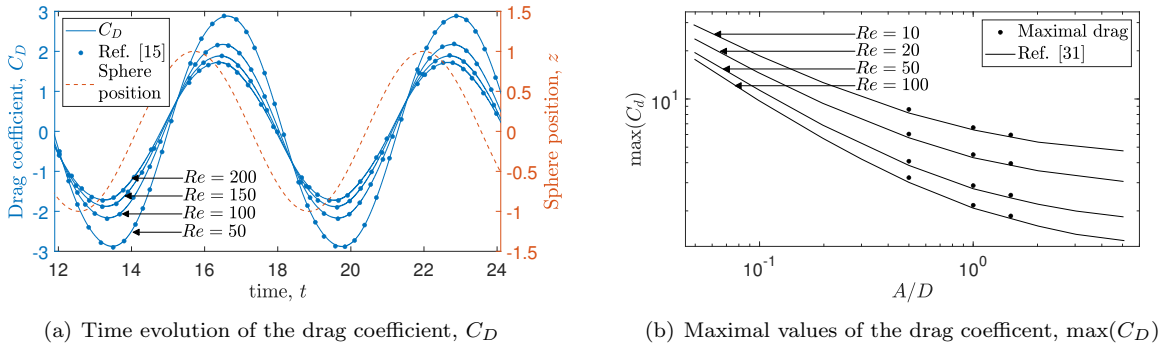


Figure 4: Time evolution of the drag coefficient  $C_D = 8f_z/\pi$  as a function of time for  $A/D = 1$ , and maximal values of the drag coefficient,  $\max(C_D)$ , as a function of  $A/D$ . The dotted line shows the position of the sphere’s center (right axis).

Iteration count for a 3D oscillating sphere						
Grid size	$Re = 10$	$Re = 20$	$Re = 50$	$Re = 100$	$Re = 200$	$Re = 300$
$50 \times 50 \times 75$	4.0	4.0	4.0	4.0	4.0	4.0
$100 \times 100 \times 150$	4.25	4.0	4.0	4.17	4.17	4.0
$200 \times 200 \times 300$	4.33	4.25	4.17	4.33	4.33	4.67
$400 \times 400 \times 600$	4.17	4.0	4.08	4.08	4.33	4.25

Table 2: Average BiCGStab iteration number for the convergence of the preconditioned system to a  $10^{-12}$  tolerance, averaged over different sphere locations and  $A/D$  ratios.

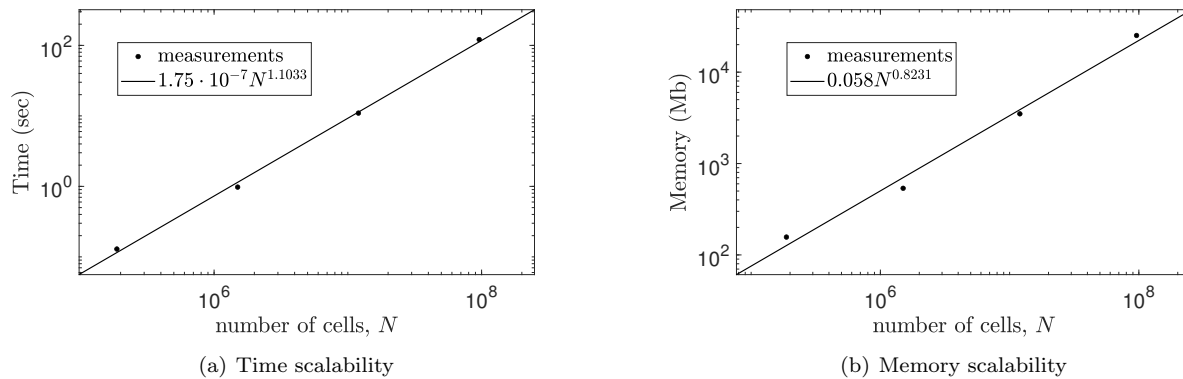


Figure 5: Wall-clock time per time-step and memory consumption for different grid sizes. The results were averaged over three  $A/D$  ratio values: 0.5, 1.0 and 1.5, and over six Reynolds number values: 10, 20, 50, 100, 200 and 300. The solid line is the linear regression line of the measurement points.

Finally, we measure the overall scalability properties of the algorithm. All the experiments were performed on a standard Linux server with 64GB DDR3 shared memory and 2 Intel Xeon 12C processors, 24 threads each (48 threads in total). Fig. 5 presents the time and memory consumption, averaged over measurements for different Reynolds numbers and different  $A/D$  ratios. A regression line was added to analyze the dependence of time and memory consumption on the grid size. Our results show that the computational

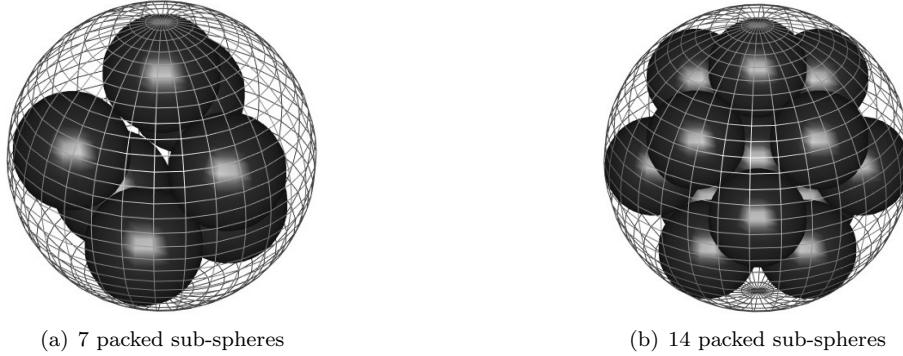


Figure 6: Schematic representation of porous spheres modeled by arrays of (a) 7 and (b) 14 solid sub-spheres packed without overlap within a bounding sphere of diameter  $D$ .

time (for a single time step) is of order  $O(N^{1.1})$ , where  $N$  is the number of cells. The results are consistent with the complexity of the direct solver from [19], as estimated in [20], i.e., the direct solver takes  $O(N^{1.33})$  in 3D, which is further decreased by using the Thomas algorithm in one of the dimensions. The results also demonstrate that the memory consumption is sub-linear. Moreover, for the largest grid examined—consisting of about 384 million unknowns—the method required only 25 GB of memory, an amount that can be found on a standard workstation and even a powerful laptop. For the sake of comparison, when the same problem was solved by [15], the memory consumption exceeded 128 GB for low  $Re$  values. The performance of our algorithm does not depend on either time step or  $Re$  values, as long as the CFL number is sufficiently small.<sup>4</sup>

### 5.3. Three-dimensional experiments: an oscillating porous sphere

In the previous subsections we have established the scalability properties of our preconditioner for the case of a single body. In this subsection we perform additional experiments to further demonstrate the capabilities of the developed method for simulation of multiple moving bodies. In the view of Remark 4.1, the number of immersed bodies might affect the sparsity of  $B$ , and thus the scattering of the eigenvalues of the preconditioned system. The aim of this subsection is to demonstrate that the same scalable behaviour holds, regardless of the number of bodies.

To this end, we focus on investigating flow properties in general and drag coefficients in particular that are typical of oscillating porous spheres. This knowledge is critical for understanding and controlling many practical applications, including the behavior of particle clusters in fluidized bed reactors, the movement of particulate matter in power generation systems, the dynamics of microcarrier transport in bioprocess applications, and the settling behavior of sediments in coastal waters [33, 34], to name a few. Following the methodology of Ma et al. [35], a porous sphere is modelled as an array of small solid sub-spheres packed without overlap within a larger bounding sphere of diameter  $D$ . The packing configuration of these small spheres is not unique and can be achieved through various approaches. For the present study, we employed the serial symmetrical relocation algorithm developed by Huang and Liang [36] to generate configurations with 7 and 14 sub-spheres.

The details regarding the radii and packing arrangements for each configuration of sub-spheres are given in Table 3. The table also includes the corresponding porosity values  $\varepsilon$ , defined as the ratio of void volume to total volume ( $\varepsilon = V_{void}/V_{total}$ ). For numerical stability in the IBM implementation, each sub-sphere’s radius was reduced by half a grid spacing to ensure proper surface contact resolution while avoiding ill-conditioning. The physical configurations of the bounding spheres, containing 7 and 14 sub-spheres, are illustrated in Figs.

<sup>4</sup>We used a CFL number that does not exceed 0.1.

7 sub-sphere configuration, $r = 0.193$ , $\varepsilon = 0.598$				14 sub-sphere configuration, $r = 0.161$ , $\varepsilon = 0.526$			
# Sub-sphere	Coordinates of sub-sphere center			# Sub-sphere	Coordinates of sub-sphere center		
	$x \times 10$	$y \times 10$	$z \times 10$		$x \times 10$	$y \times 10$	$z \times 10$
1	1.1140	-1.9296	-2.1126	1	0	-2.287	-2.4917
2	-2.2281	0	-2.1126	2	-2.2875	0	-2.4917
3	1.1140	1.9296	-2.1126	3	2.2875	0	-2.4917
4	-1.5009	-2.5997	0.64522	4	0	2.2875	-2.4917
5	3.0019	0	0.64522	5	-2.3820	-2.3820	-0.30478
6	-1.5009	2.5997	0.64522	6	2.3820	-2.3820	-0.30478
7	0	0	3.0704	7	-2.3820	2.3820	-0.30478
				8	2.3820	2.3820	-0.30478
				9	0	0	0
				10	0	-2.8412	1.8355
				11	-2.8412	0	1.8355
				12	2.8412	0	1.8355
				13	0	2.8412	1.8355
				14	0	0	3.3825

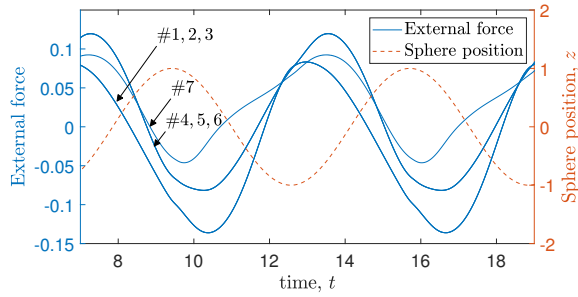
Table 3: Center coordinates of 7 and 14 sub-spheres constituting the model of a bounding sphere of diameter  $D$ . Here  $r$  is the radius of sub-spheres normalized by  $D$ , and  $\varepsilon$  is the corresponding porosity. The center of the bounding sphere is located at the origin of the coordinate system.

6(a) and 6(b), respectively. A spherical wire-frame is shown in these figures to indicate the boundary of the theoretical bounding sphere.

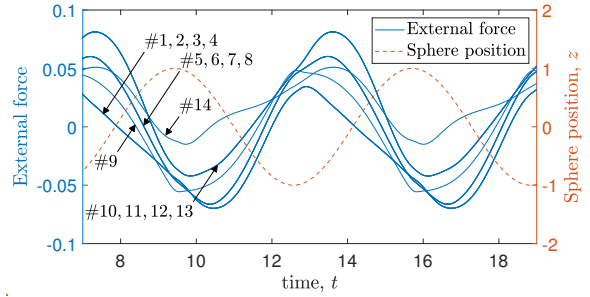
To understand the dynamics of the system, we analyze the external forces (calculated using Eq. (35)) required to drive the oscillatory motion of each sub-sphere. Figure 7 presents the temporal evolution of these external forces (left axis) for the 7 sub-sphere and 14-sphere arrays under three different Reynolds numbers:  $Re = 100$ ,  $Re = 200$ , and  $Re = 300$ . The dotted line represents the temporal evolution of the  $z$ -coordinate of the bounding sphere’s center (right axis).

The analysis of Figs. 7(a), 7(c) and 7(e) demonstrates that sub-spheres experience different temporal forces, with their magnitudes and patterns determined by vertical position within the bounding sphere. Sub-spheres at equal vertical positions experience identical temporal forces regardless of their horizontal coordinates, confirming the axial nature of the force distribution. The temporal evolution of forces on individual sub-spheres exhibits clear asymmetry, quantified by differences between positive and negative force peaks. Sub-spheres #1, #2, and #3, positioned below the bounding sphere’s center, experience negative forces approximately 50% larger than their positive counterparts during downward motion, with reduced forces during upward motion due to shielding from upper sub-spheres. Sub-sphere #7, positioned at the top edge of the bounding sphere, displays an inverse asymmetry pattern, with positive force peaks exceeding negative values by approximately 40%. Sub-spheres #4, #5, and #6, located slightly above the center and attached to the outer boundary of the bounding sphere, remain unshielded by other sub-spheres throughout the oscillation cycle. This unshielded position results in nearly symmetric forces about zero, with peak-to-peak variations not exceeding 10%. The magnitude of these forces systematically decreases with increasing Reynolds number across all cases, while maintaining consistent phase relationships relative to the bounding sphere’s position. This reduction in force amplitude demonstrates the diminishing effect of viscous forces at higher Reynolds numbers, though the fundamental force distribution patterns persist.

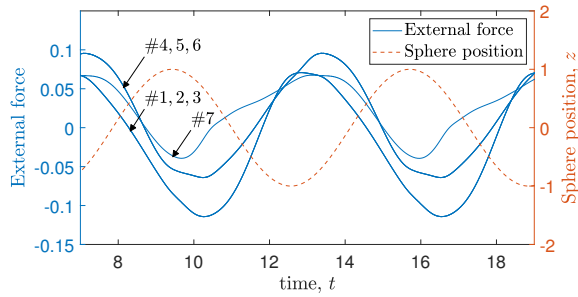
The behavior of external forces in the case of 14 sub-spheres exhibits similar patterns while revealing additional features due to the more complex internal structure. The analysis of Figs. 7(b), 7(d) and 7(f) confirms that sub-spheres at equal vertical positions experience identical temporal forces regardless of their horizontal coordinates. Sub-spheres #1 through #4, positioned at  $z \approx -0.249$  below the bounding sphere’s center, experience negative forces approximately 45% larger than their positive counterparts during



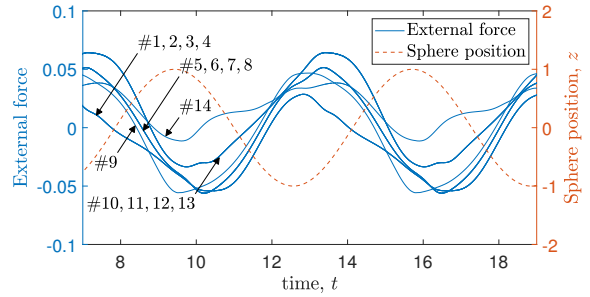
(a)  $Re = 100$ , 7 sub-spheres



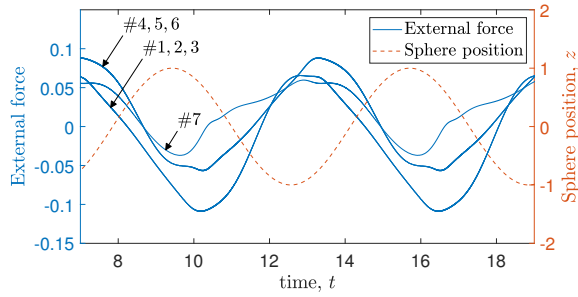
(b)  $Re = 100$ , 14 sub-spheres



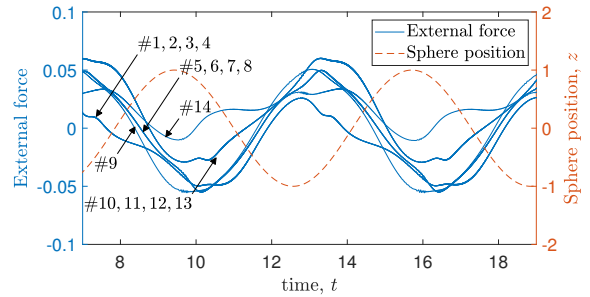
(c)  $Re = 200$ , 7 sub-spheres



(d)  $Re = 200$ , 14 sub-spheres



(e)  $Re = 300$ , 7 sub-spheres



(f)  $Re = 300$ , 14 sub-spheres

Figure 7: Time evolution of external forces applied to individual sub-spheres in the 7-sphere array and in the 14-sphere array during oscillatory motion. Each solid curve corresponds to the force applied to a sub-sphere identified by its serial number from Table 3.

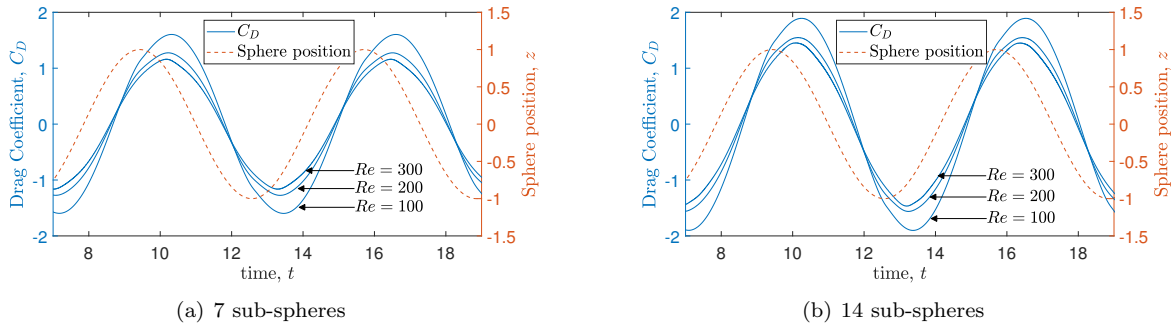


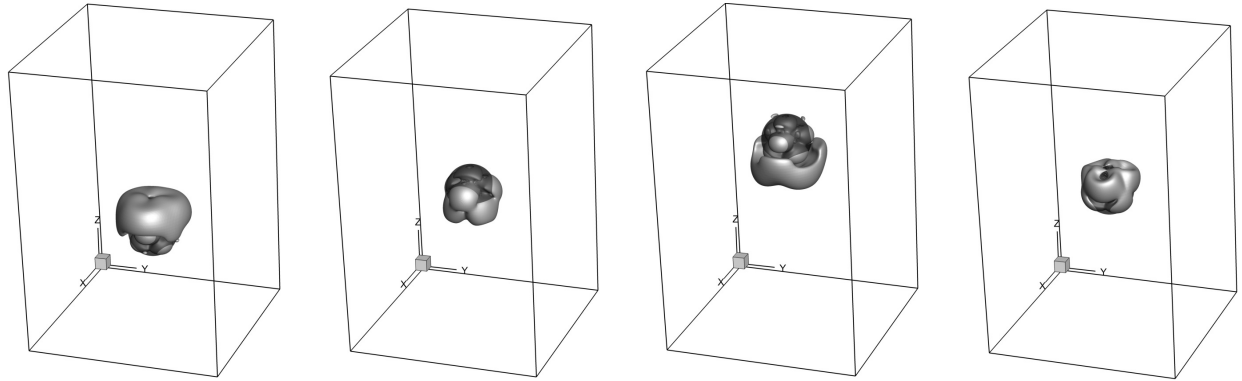
Figure 8: Time evolution of the total drag coefficient,  $C_D$  obtained for the values of  $Re = 100, 200$  and  $300$ .

downward motion, with reduced forces during upward motion due to shielding from upper sub-spheres. Sub-spheres #5 through #8, located near the equatorial plane at  $z \approx -0.030$ , show intermediate behavior with force asymmetry less pronounced than for the bottom spheres. Their position, slightly below the geometric center, results in force patterns that reflect partial shielding effects from both upper and lower neighboring spheres. The force distribution of sphere #9, uniquely positioned at the exact geometric center ( $z = 0$ ) of the confining sphere, demonstrates nearly symmetric behavior about zero, with peak-to-peak variations not exceeding 5%, due to balanced shielding from surrounding sub-spheres. Sub-spheres #10 through #13, located at  $z \approx 0.184$ , display moderate force asymmetry with positive peaks approximately 30% larger than negative ones. Sub-sphere #14, positioned at  $z \approx 0.338$  at the top edge of the bounding sphere, exhibits the strongest asymmetry in the upper region, with positive force peaks exceeding negative values by approximately 35%. As in the previous case, these asymmetric force patterns persist across all examined  $Re$  values, with diminishing magnitudes at higher Reynolds numbers.

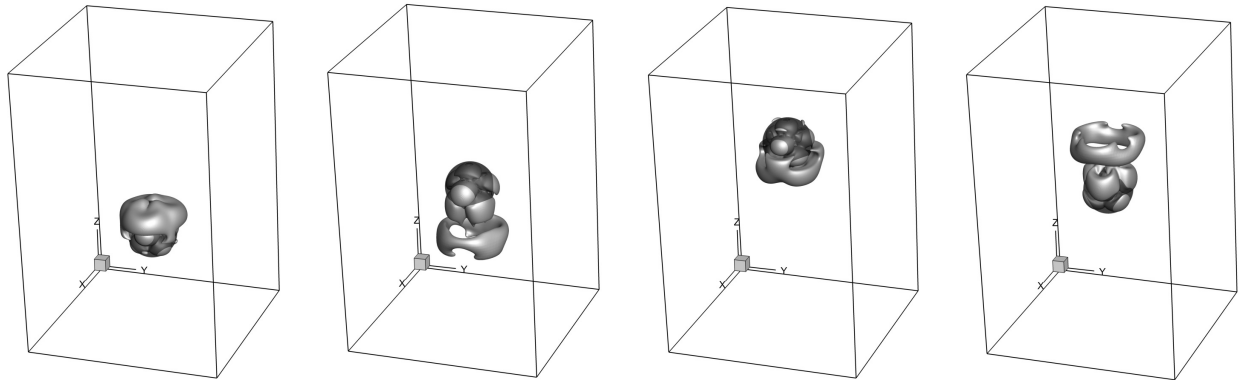
We next analyze the total drag coefficients,  $C_D$ , for arrays consisting of 7 and 14 sub-spheres. These coefficients are calculated by summing the drag forces in the  $z$  direction acting on each sub-sphere within the corresponding array and multiplying by a factor of  $8/\pi$  (see Eq. (37)). The time evolution of  $C_D$ , calculated for arrays consisting of 7 and 14 sub-spheres, is shown in Fig. 8.

Looking at Fig. 8, we observe three key trends in the drag coefficient evolution. First, the magnitude of  $C_D$  systematically decreases with increasing Reynolds numbers, for both 7 and 14 sub-sphere arrays. This trend directly reflects diminishing viscous effects at higher  $Re$  values, resulting in reduced drag forces. Second, the 14 sub-sphere configuration exhibits consistently higher  $C_D$  values compared to the 7 sub-sphere array across all Reynolds numbers, approaching the drag coefficient values that characterize a non-porous sphere, as reported in our previous work (see [15], Fig. 7). This behavior is expected, as increasing the number of sub-spheres reduces the array's porosity, making it more similar to a solid sphere. Third, a persistent phase lag exists between the sphere position and drag coefficient evolution. This phase lag arises from the fundamental relationship between force and motion in oscillatory flows: the drag force is primarily dependent on the velocity rather than the displacement. At low  $Re$  values, the force reaches its maximum when the velocity is highest (at zero displacement) and its minimum when the velocity is zero (at maximum displacement), creating an inherent quarter-period phase shift. This kinematic relationship persists across all  $Re$  values, with additional inertial effects becoming more pronounced at higher Reynolds numbers but not altering the basic phase relationship. Note that a similar phase lag is present in Fig. 4 from the previous subsection, corresponding to a single oscillating sphere.

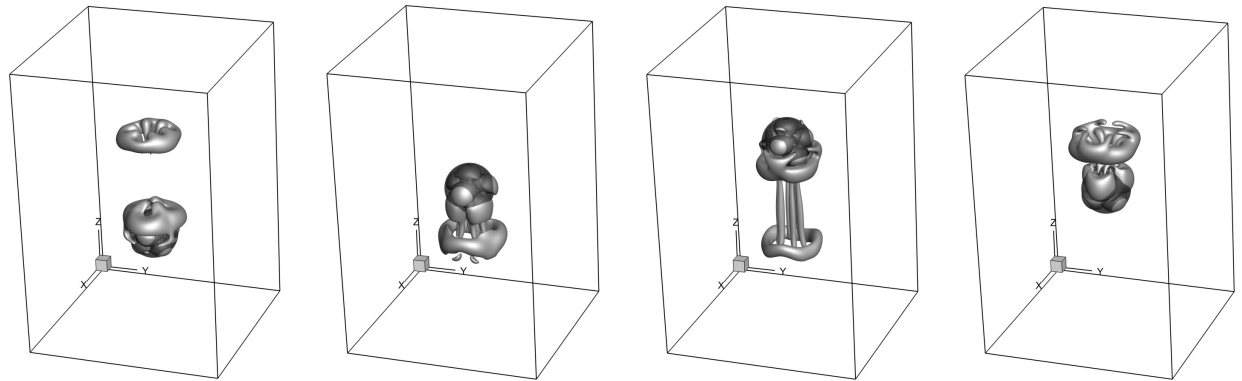
To gain deeper insight into the fluid dynamics associated with the transverse motion of porous spheres, we visualize the vortical structures generated by the flow. The visualization utilizes isosurfaces of the  $Q$ -criterion ( $Q = 0.05$ ), where  $Q$  represents the second invariant of the velocity gradient tensor. This value of  $Q$  was chosen to effectively capture coherent vortical structures while filtering out weaker vorticity regions, thereby highlighting the dominant flow features. The evolution of vortical structures over one oscillation



(a) Isosurfaces of the  $Q = 0.05$  criterion for  $Re = 100$ , calculated at different points of the sphere's trajectory: the lowest point, mid-point on the way up, highest point and mid-point on the way down (from left to right)

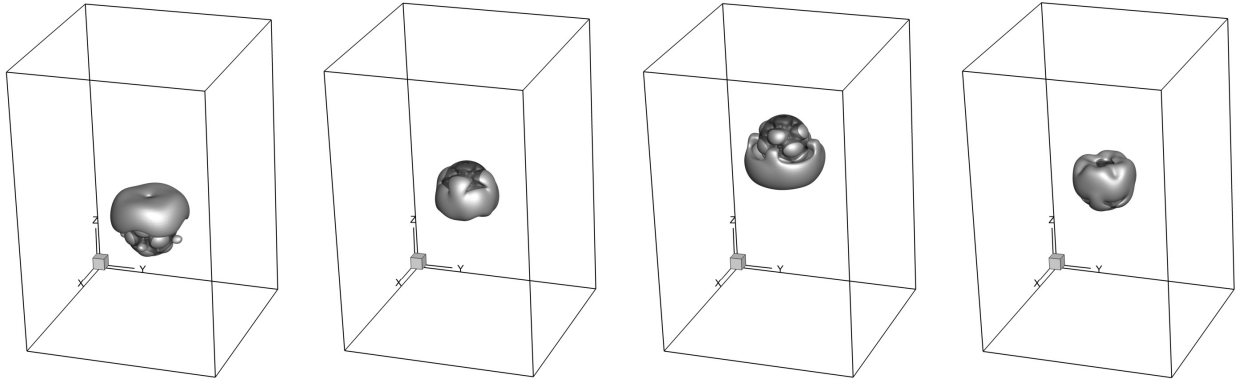


(b) Isosurfaces of the  $Q = 0.05$  criterion for  $Re = 200$ , calculated at different points of the sphere's trajectory: the lowest point, mid-point on the way up, highest point and mid-point on the way down (from left to right)

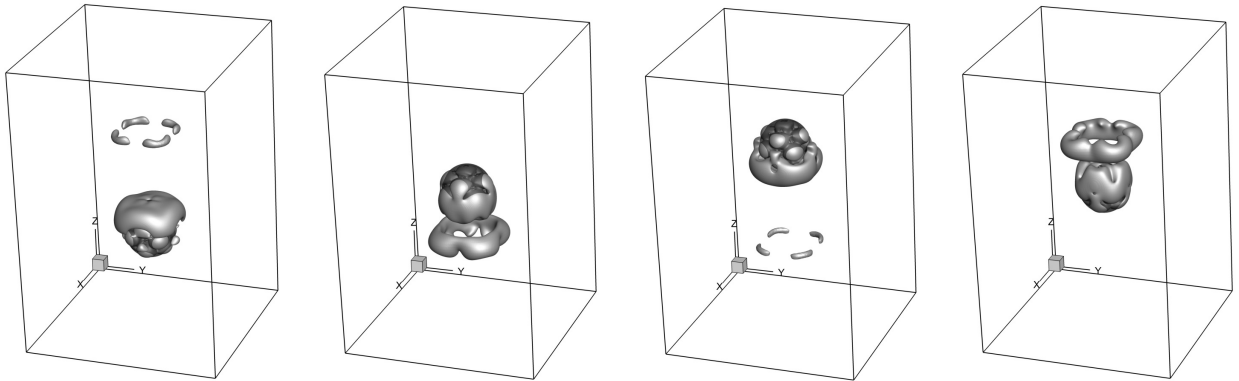


(c) Isosurfaces of the  $Q = 0.05$  criterion for  $Re = 300$ , calculated at different points of the sphere's trajectory: the lowest point, mid-point on the way up, highest point and mid-point on the way down (from left to right)

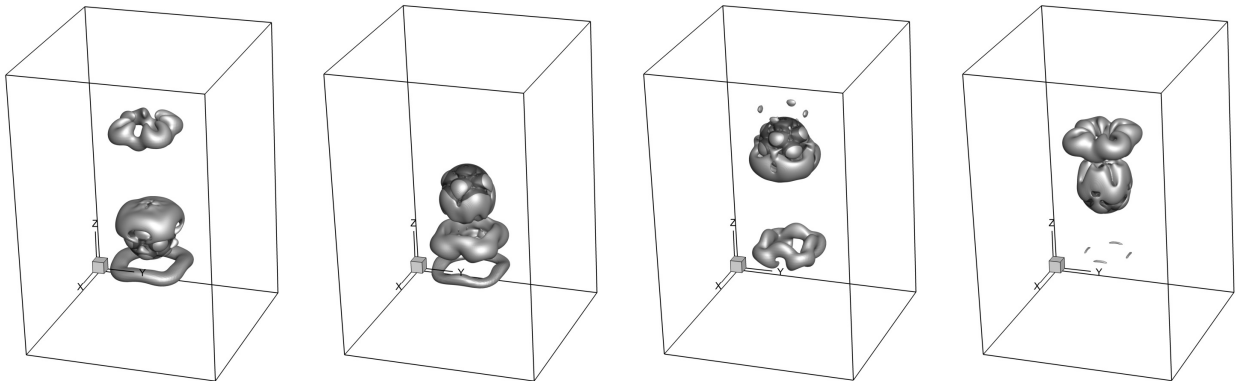
Figure 9: Visualization of vortical structures (isosurfaces of  $Q = 0.05$ ) generated by a transversely oscillating sphere over a single oscillation period, calculated for  $Re = 100, 200,$  and  $300$  at  $A/D = 1$ . The bounding sphere containing 7 sub-spheres is indicated by a semitransparent surface.



(a) Isosurfaces of the  $Q = 0.05$  criterion for  $Re = 100$ , calculated at different points of the sphere's trajectory: the lowest point, mid-point on the way up, highest point and mid-point on the way down (from left to right)



(b) Isosurfaces of the  $Q = 0.05$  criterion for  $Re = 200$ , calculated at different points of the sphere's trajectory: the lowest point, mid-point on the way up, highest point and mid-point on the way down (from left to right)



(c) Isosurfaces of the  $Q = 0.05$  criterion for  $Re = 300$ , calculated at different points of the sphere's trajectory: the lowest point, mid-point on the way up, highest point and mid-point on the way down (from left to right)

Figure 10: Visualization of vortical structures (isosurfaces of  $Q = 0.05$ ) generated by a transversely oscillating sphere over a single oscillation period, calculated for  $Re = 100, 200$ , and  $300$  at  $A/D = 1$ . The bounding sphere containing 14 sub-spheres is indicated by a semitransparent surface.

period is shown in Figs. 9 and 10 for configurations containing 7 and 14 sub-spheres, respectively. In both configurations, a clear Reynolds number dependence is observed in the persistence of vortical structures. At  $Re = 100$ , vortices dissipate rapidly due to dominant viscous diffusion. As  $Re = 300$ , vortical structures maintain their coherence over longer periods and travel further from the sphere surface before dissipating, reflecting the diminishing role of viscous effects relative to inertial forces.

A notable distinction between the two configurations lies in their flow penetration characteristics. The 7 sub-sphere array, with its higher porosity, exhibits more pronounced flow penetration between sub-spheres, manifested in elongated vortical structures that extend through the array (Fig. 9). In contrast, the 14 sub-sphere configuration shows more compact vortical structures that primarily develop around the array’s outer boundary (Fig. 10), consistent with its lower porosity. This difference is particularly evident at  $Re = 300$ , where the vortical structures in the 7 sub-sphere case show distinct columnar formations that are absent in the denser 14 sub-sphere arrangement. Additionally, both configurations demonstrate asymmetric vortex shedding patterns between upward and downward motions, with more intense vortex formation occurring during direction reversal at the trajectory extrema. This asymmetry becomes more pronounced with increasing Reynolds number, particularly visible in the higher resolution structures at  $Re = 300$ .

After testing our accelerated SIMPLE-IBM on multiple sub-sphere arrays, we demonstrate that our solver’s performance scales independently of the number of sub-spheres. Table 4 shows the BiCGStab iteration count needed to solve Eq. (19) with preconditioning, averaged over a single oscillation period, for different Reynolds numbers ( $Re=50, 100, 200$ , and  $300$ ) and grid resolutions. The results show that this period-averaged iteration count remains nearly constant, requiring 4-5 iterations for both 7 and 14 sub-sphere configurations. Furthermore, these period-averaged iteration counts match the results in Table 2 for a single oscillating sphere, demonstrating consistent performance across different configurations. These numerical results, combined with Theorem 4.1, demonstrate our method’s applicability and scalability across a wide range of applications.

Iteration count for a 3D porous sphere								
Grid size	7 sub-spheres configuration				14 sub-spheres configuration			
	$Re = 50$	$Re = 100$	$Re = 200$	$Re = 300$	$Re = 50$	$Re = 100$	$Re = 200$	$Re = 300$
$100 \times 100 \times 150$	4.59	4.48	4.66	4.64	4.74	4.74	4.79	4.76
$200 \times 200 \times 300$	4.94	4.96	4.95	4.95	4.98	4.98	4.98	4.93
$400 \times 400 \times 600$	4.81	4.82	4.82	4.87	4.97	4.98	4.98	5.00

Table 4: Period-averaged BiCGStab iteration count for solving the preconditioned system at different Reynolds numbers and grid resolutions, with convergence tolerance of  $10^{-12}$ . Results shown for configurations with 7 and 14 sub-spheres, for  $A/D = 1$ .

## 6. Conclusion and future work

We present a novel, scalable direct-forcing IBM for efficient moving boundary simulations that builds upon the SIMPLE-IBM method [16]. To address the pressure-forces coupling, a block reduction technique is applied to solve for the pressure corrections first, taking the Laplacian as a preconditioner for the resulting primal Schur complement. We prove rigorously and show numerically that the Laplacian is spectrally equivalent to the primal Schur complement. This key observation enables an efficient and robust method, as the pressure’s Laplacian, being independent of the coordinates of the immersed body, needs to be factorized only once—using a fast direct method [19]—and can then be reused throughout the simulation.

We prove theoretically and demonstrate numerically that the efficiency of our approach does not depend on the grid resolution or on the number of moving bodies, thereby ensuring excellent scalability in time and memory consumption. This leads to notably low memory requirements, enabling precise moving boundary simulations (that often require high-performance computing facilities) to run on standard workstations or even laptops. Consequently, our approach enhances the accessibility of advanced moving boundary simulations to the CFD community. In this work, we examined the applicability of the method in a one-way

coupled FSI framework. The methodology was successfully verified by simulating flows generated by a transversely oscillating sphere, showing good agreement with previously published results for various Reynolds numbers and oscillation amplitudes. The verified approach was then extended to more challenging configurations involving multiple moving bodies, specifically analyzing porous spheres modelled as arrays multiple sub-spheres. The simulations revealed distinct flow characteristics associated with different array porosities, including variations in drag coefficients, phase relationships, and vortical structure evolution, while maintaining computational stability and accuracy throughout all investigated parameters.

Future research directions should extend the method to two-way coupled FSI problems, specifically for the simulation of undulatory swimming and particle-laden flows. The efficiency of our preconditioner is independent of the specific discrete delta functions used, allowing for further improvements in accuracy through delta functions with a wider support [6]. As we approximate the regularization block by a scalar matrix, a key challenge lies in identifying delta functions with sufficiently wide support, for which the regularization block can still be well approximated by a scalar matrix.

Finally, our method employs a direct solver [19] designed for homogeneous boundary conditions. While this limitation is not particularly restrictive for our current application (as we use it to solve the Poisson equation for pressure corrections, typically formulated with homogeneous boundary conditions), there is potential for further generalization by applying, for example, a geometric multigrid [37] V-cycle to the Poisson equation in each preconditioning step, rather than a direct solution. Subtle fine-tuning of the multigrid method might also yield linear time scaling. The above-described enhancements would further increase the versatility of our approach for a wider range of FSI problems and enable better spatial accuracy.

### **CRedit authorship contribution statement**

Rachel Yovel: analysis and related examples, validation, writing.

Eran Treister: supervision, validation, writing.

Yuri Feldman: supervision, software, validation, writing.

### **Declaration of competing interest**

The authors declare that they have no known competing financial interests or personal relationships that could have appeared to influence the work reported in this paper.

### **Funding**

This research was supported by the Israel Science Foundation, Grant No. 656/23, and by the Lynn and William Frankel Center for Computer Science at BGU. The second author is also supported by the Ariane de Rothschild scholarship and by the Kreitman High-tech scholarship. The third author is supported by the Israel Ministry of Energy and Infrastructure (grant No. 222-11-049).

### **References**

- [1] C. S. Peskin, Flow patterns around heart valves: a numerical method, *Journal of computational physics* 10 (2) (1972) 252–271.
- [2] R. Verzicco, Immersed boundary methods: Historical perspective and future outlook, *Annual Review of Fluid Mechanics* 55 (2023) 129–155.
- [3] J. Mohd-Yusof, Combined immersed-boundary/b-spline methods for simulations of flow in complex geometries, Center for Turbulence Research, *Annual Research Briefs* (1997) 317–327.
- [4] A. Faldun, E., R. Verzicco, P. Orlandi, J. Mohd-Yusof, Combined immersed-boundary finite-difference methods for three-dimensional complex flow simulations, *J. Comput. Phys.* 161 (1) (2000) 35–60.

- [5] D. B. Stein, R. D. Guy, B. Thomases, Immersed boundary smooth extension: a high-order method for solving pde on arbitrary smooth domains using fourier spectral methods, *Journal of Computational Physics* 304 (2016) 252–274.
- [6] D. B. Stein, R. D. Guy, B. Thomases, Immersed boundary smooth extension (ibse): a high-order method for solving incompressible flows in arbitrary smooth domains, *Journal of Computational Physics* 335 (2017) 155–178.
- [7] I. N. Yildiran, N. Beratlis, F. Capuano, Y.-H. Loke, K. Squires, E. Balaras, Pressure boundary conditions for immersed-boundary methods, *Journal of Computational Physics* 510 (2024) 113057.
- [8] E. Farah, A. Ouahsine, P. G. Verdin, An improved implicit direct-forcing immersed boundary method (df-ibm) around arbitrarily moving rigid structures, *Physics of Fluids* 36 (10) (2024).
- [9] Y. Bao, A. Donev, B. E. Griffith, D. M. McQueen, C. S. Peskin, An immersed boundary method with divergence-free velocity interpolation and force spreading, *Journal of Computational Physics* 347 (2017) 183–206.
- [10] S. Liska, T. Colonius, A fast immersed boundary method for external incompressible viscous flows using lattice green’s functions, *Journal of Computational Physics* 331 (2017) 257–279.
- [11] J. D. Eldredge, A method of immersed layers on cartesian grids, with application to incompressible flows, *Journal of Computational Physics* 448 (2022) 110716.
- [12] Y. Mori, C. S. Peskin, Implicit second-order immersed boundary methods with boundary mass, *Computer methods in applied mechanics and engineering* 197 (25-28) (2008) 2049–2067.
- [13] T. Y. Hou, Z. Shi, An efficient semi-implicit immersed boundary method for the navier–stokes equations, *Journal of Computational Physics* 227 (20) (2008) 8968–8991.
- [14] Y. Feldman, Semi-implicit direct forcing immersed boundary method for incompressible viscous thermal flow problems: a schur complement approach, *International Journal of Heat and Mass Transfer* 127 (2018) 1267–1283.
- [15] R. Sela, E. Zemach, Y. Feldman, A semi-implicit direct forcing immersed boundary method for periodically moving immersed bodies: A schur complement approach, *Computer Methods in Applied Mechanics and Engineering* 373 (2021) 113498.
- [16] K. Goncharuk, O. Oshri, Y. Feldman, The immersed boundary method: A simple approach, *Journal of Computational Physics* 487 (2023) 112148.
- [17] K. Taira, T. Colonius, The immersed boundary method: a projection approach, *Journal of Computational Physics* 225 (2) (2007) 2118–2137.
- [18] Q. Zhang, R. D. Guy, B. Philip, A projection preconditioner for solving the implicit immersed boundary equations, *Numerical Mathematics: Theory, Methods and Applications* 7 (4) (2014) 473–498.
- [19] R. E. Lynch, J. R. Rice, D. H. Thomas, Direct solution of partial difference equations by tensor product methods, *Numerische Mathematik* 6 (1964) 185–199.
- [20] H. Vitoshkin, A. Y. Gelfgat, On direct and semi-direct inverse of stokes, helmholtz and laplacian operators in view of time-stepper-based newton and arnoldi solvers in incompressible cfd, *Communications in Computational Physics* 14 (4) (2013) 1103–1119.
- [21] A. M. Roma, C. S. Peskin, M. J. Berger, An adaptive version of the immersed boundary method, *Journal of computational physics* 153 (2) (1999) 509–534.
- [22] M. Uhlmann, An immersed boundary method with direct forcing for the simulation of particulate flows, *Journal of computational physics* 209 (2) (2005) 448–476.
- [23] T. Kempe, J. Fröhlich, An improved immersed boundary method with direct forcing for the simulation of particle laden flows, *Journal of Computational Physics* 231 (9) (2012) 3663–3684.

- [24] S. V. Patankar, D. B. Spalding, A calculation procedure for heat, mass and momentum transfer in three-dimensional parabolic flows, in: Numerical prediction of flow, heat transfer, turbulence and combustion, Elsevier, 1983, pp. 54–73.
- [25] P. Amestoy, I. Duff, J. LéExcellent, J. Koster, A fully asynchronous multifrontal solver using distributed dynamic scheduling, *SIAM J. Matrix Anal. Appl.* 23 (2001) 15–41.
- [26] H. A. Van der Vorst, Bi-cgstab: A fast and smoothly converging variant of bi-cg for the solution of nonsymmetric linear systems, *SIAM Journal on scientific and Statistical Computing* 13 (2) (1992) 631–644.
- [27] H. C. Elman, D. J. Silvester, A. J. Wathen, *Finite elements and fast iterative solvers: with applications in incompressible fluid dynamics*, Oxford university press, 2014.
- [28] Y. Saad, *Numerical methods for large eigenvalue problems: revised edition*, SIAM, 2011.
- [29] W.-P. Breugem, A second-order accurate immersed boundary method for fully resolved situations of particle-laden flows, *J. Comput. Phys.* 231 (2012) 4469–4498.
- [30] M. Uhlmann, An immersed boundary method with direct forcing for the simulation of particulate flows, *Journal of Computational Physics* 209 (2005) 448–476.
- [31] H. M. Blackburn, Mass and momentum transport from a sphere in steady and oscillatory flows, *Physics of fluids* 14 (11) (2002) 3997–4011.
- [32] P. Leopardi, A partition of the unit sphere into regions of equal area and small diameter, *Electronic Transactions on Numerical Analysis* 25 (2006) 309–327.
- [33] C. Li, M. Ye, Z. Liu, On the rotation of a circular porous particle in 2D simple shear flow with fluid inertia, *Journal of Fluid Mechanics* 808 (2016) R3.
- [34] P. Yu, Y. Zeng, T. Lee, X. Chen, H. Low, Numerical simulation on steady flow around and through a porous sphere, *International Journal of Heat and Fluid Flow* 36 (2012) 142–152.
- [35] L. Ma, S. Xu, X. Li, Q. Guo, D. Gao, Y. Ding, M. Ye, Z. Liu, Particle tracking velocimetry of porous sphere settling under gravity: Preparation of the model porous particle and measurement of drag coefficients, *Powder Technology* 360 (2020) 241–252.
- [36] W. Huang, Y. Liang, Serial symmetrical relocation algorithm for the equal sphere packing problem, *arXiv preprint arXiv:1202.4149* (2012).
- [37] A. Brandt, Multi-level adaptive solutions to boundary-value problems, *Mathematics of computation* 31 (138) (1977) 333–390.